The Astrophysical Journal, 657:30–36, 2007 March 1


# CLUSTER-SUPERCLUSTER ALIGNMENTS

Jounghun Lee[1] and August E. Evrard[2,3,4]
*Received 2006 August 30; accepted 2006 November 17*

## ABSTRACT

We study correlations in spatial orientation between galaxy clusters and their host superclusters using a Hubble volume *N*-body realization of a concordance cosmology and an analytic model for tidally induced alignments. We derive an analytic form for the distributions of alignment angle as functions of halo mass ($M$), ellipticity ($\epsilon$), distance ($r$), and velocity ($v$) and show that the model, after tuning of three parameters, provides a good fit to the numerical results. The parameters indicate a high degree of alignment along anisotropic, collapsed filaments. The degree of alignment increases with $M$ and $\epsilon$, while it decreases with $r$ and is independent of $v$. We note the possibility of using the cluster-supercluster alignment effect as a cosmological probe to constrain the slope of the initial power spectrum.

*Subject headings:* cosmology: theory — large-scale structure of universe

## 1. INTRODUCTION

Superclusters are collections of galaxy groups and clusters that represent the largest gravitationally bound structures in the universe (Shapley 1930; Kalinkov et al. 1998). If the dark energy is a cosmological constant, then the collapse of these systems over the next few billion years of the cosmic future will mark the end of hierarchical structure formation in our universe (Nagamine & Loeb 2003; Busha et al. 2005). A conspicuous feature of locally observed superclusters is the strong tendency of member clusters to be elongated along their major-axis orientations (Plionis 2002, 2004), which is in turn closely related to their filamentary shapes (see, e.g., Basilakos 2003). To describe the structure distribution on the largest scale in the universe, it is quite essential to understand this effect of cluster-supercluster alignments from first principles.

The effect of structure-substructure alignment is in fact observed on all different scales in the universe. On the subgalactic scale, galaxy satellites are observed to preferentially be located near the major axes of their host galaxies (Valtonen et al. 1978; Knebe et al. 2004; Brainerd 2005; Agustsson & Brainerd 2006). On the galactic scale, the major axes of cluster galaxies are observed to be aligned with those of their host clusters (Plionis & Basilakos 2002; Plionis et al. 2003). The cluster galaxies are also observed to have a strong tendency toward radial alignment (Pereira & Kuhn 2005).

Although this alignment effect has been shown to be a natural outcome in the currently favored concordance ΛCDM cosmology (Onuora & Thomas 2000; Libeskind et al. 2005; Kang et al. 2005; Lee et al. 2005; Zentner et al. 2005; Kasun & Evrard 2005; Basilakos et al. 2006), the details of its origin remain a subject of debate between those who emphasize the importance of anisotropic merging and those who stress tidal interaction.

The anisotropic-merging scenario explains the effect of substructure-structure alignment as being induced by the anisotropic merging and infall of matter along filaments (West 1989). It has indeed been shown by *N*-body simulations that the merging and infall of matter to form bound halos occur preferentially along filaments, which provides supporting evidence for this scenario (e.g., West et al. 1991; van Haarlem & van de Weygaert 1993; Dubinski 1998; Faltenbacher et al. 2002; Knebe et al. 2004; Zentner et al. 2005).

The tidal interaction theory explains that the correlations between the substructure angular momentum vectors and the principal axes of the host tidal fields induce the alignment effect. Lee et al. (2005) constructed an analytic model for the effect of substructure alignment in the frame of the tidal interaction theory and showed that their analytic predictions are in good agreement with the numerical results from *N*-body simulations.

In fact, the above two theories are not mutually exclusive, since the anisotropic merging and infall itself is a manifestation of the primordial tidal field (Bond et al. 1996). The difference between the two scenarios, however, lies in the question whether the connection to filaments is a major contribution or not.

Very recently, Atlay et al. (2006) have quantified the influences of both the tidal interaction and the anisotropic infall through analysis of data from recent high-resolution *N*-body simulations. What they confirmed is the following: (1) for the majority of halos, the alignment effect is caused by the tidal field but not by the anisotropic infall, and (2) only for cluster-size halos is the alignment effect predominantly due to the anisotropic merging and infall of matter along filaments. In other words, they made it clear that the filaments are important markers of local orientation on the cluster halo scale.

Now that cluster-supercluster alignment has turned out to be due to anisotropic merging along filaments, it is desirable to have a theoretical framework within which one can provide physical answers to the remaining questions, such as how the alignment effect depends on the cluster properties such as mass, shape, etc. Our goal here is to construct such a theoretical framework by using both analytical and numerical methods. Analytically we adopt the standard cosmic-web theory, and numerically we use data from a large Hubble volume simulation.

The organization of this paper is as follows: In § 2, we provide a brief description of the Hubble volume simulation and summarize

[1] Frontier Physics Research Division, Department of Physics and Astronomy, Seoul National University, Seoul, Korea.
[2] Department of Astronomy and Michigan Center for Theoretical Physics, University of Michigan, Ann Arbor, MI.
[3] Department of Physics and Michigan Center for Theoretical Physics, University of Michigan, Ann Arbor, MI.
[4] Visiting Miller Professor, Department of Physics, University of California, Berkeley, CA.

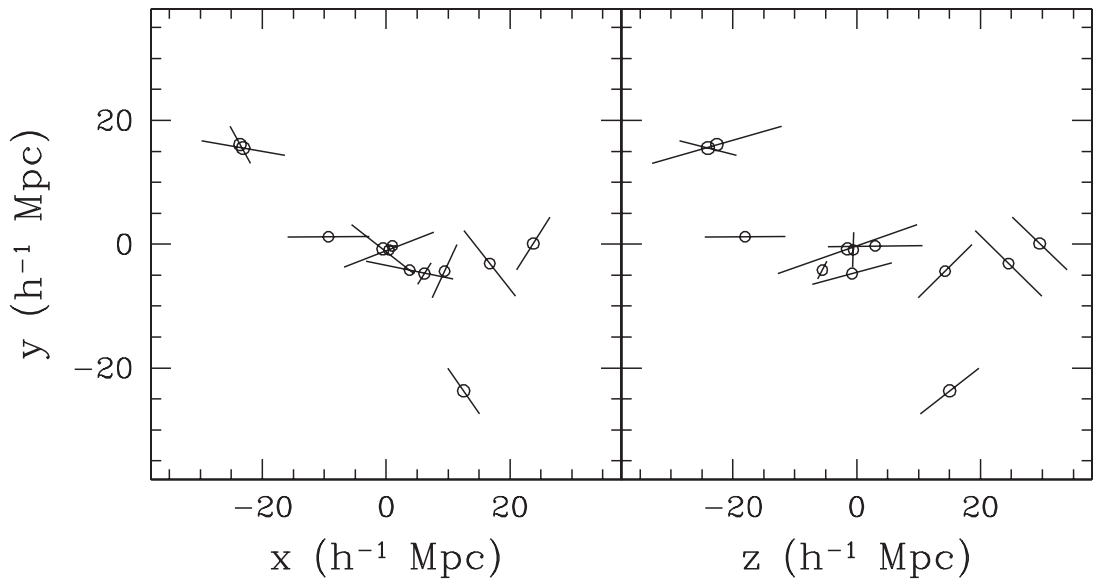


FIG. 1.—Spatial distribution of the third-richest supercluster, shown in orthogonal projections. Circles show halo locations, with symbol size scaling as $M^{1/3}$, while the lines through each halo show the orientation of the major axis of its density field, taken from Kasun & Evrard (2005). The length of each line is proportional to the halo's major-to-minor axis ratio.

the numerical results. In § 3, we present an analytic model and compare its predictions with the numerical results. In § 4, we discuss our results and draw final conclusions.

## 2. NUMERICAL RESULTS

For the numerical analysis, we use a mass-limited sample of cluster halos extracted from the Hubble volume simulation of a ΛCDM universe (Evrard et al. 2002). The simulation models dark matter structure resolved by particles of mass $m = 2.25 \times 10^{12}\, h^{-1}\, M_\odot$ in a periodic cube of linear size 3000 $h^{-1}$ Mpc, assuming $\Omega_m = 0.3$, $\Omega_\Lambda = 0.7$, and $\sigma_8 = 0.9$. The $z = 0$ catalog contains a total of 82,973 halos with mass $M$ above a limiting value of $3 \times 10^{14}\, h^{-1}\, M_\odot$, with information on various properties such as center-of-mass position, mass, inertia momentum tensor, and redshift. We refer the readers to Evrard et al. (2002) and Kasun & Evrard (2005) for the details of the cluster catalog, including the algorithm for cluster identification.

The superclusters are identified in the catalog with the help of the friends-of-friends algorithm with a linking length of $0.33\bar{l}$, where $\bar{l} = 69\, h^{-1}$ Mpc is the mean spacing of the mass-limited sample. The total number and the mean mass of the identified superclusters are $N_s = 14{,}007$ and $\bar{M}_s = 1.26 \times 10^{15}\, h^{-1}\, M_\odot$, respectively. This large number of superclusters allows us to study the alignment effect with high statistical power.

Figure 1 shows orthogonal projections of the third-richest supercluster in the volume. It contains 12 halos above the applied mass limit and a total mass of $5.3 \times 10^{15}\, h^{-1}\, M_\odot$ associated with these halos. The spatial distribution of the supercluster is highly elongated, much closer to filamentary than spherical. In this example, the major-axis orientations of the halos, taken from Kasun & Evrard (2005), are shown as whiskers in the plot. The tendency for these halos to be aligned with their supercluster's principal axis, although arguably visible in this plot, is a weak effect. We therefore seek a statistical measure using the entire supercluster sample.

For each supercluster, we measure its inertia momentum tensor, $\mathbf{I}^s \equiv (I^s_{ij})$, as

$$I^s_{ij} = \frac{1}{M_s} \sum_\alpha M^\alpha_c\, x^\alpha_{c,i} x^\alpha_{c,j}, \qquad (1)$$

where $M^\alpha_c$ and $\boldsymbol{x}^\alpha_c \equiv (x^\alpha_{c,i})$ represent the mass and position of the $\alpha$th member cluster, respectively, and $M_s$ is the total mass of the host supercluster. Then we compute the eigenvalues and eigenvectors through the diagonalization of $\mathbf{I}^s$ and determine the major-axis direction as the direction of the eigenvector corresponding to the largest eigenvalue.

It is however worth mentioning here that for a supercluster that has fewer than five clusters, the orientation of its major axis derived using equation (1) must suffer from considerable inaccuracy. The most idealistic technique would be to derive the major axis of a supercluster using all particles within it.

Nevertheless, given that the major axes of the superclusters in real observations cannot be determined in this idealistic way, because the positions of the dark matter particles are not measurable, the advantage of our analysis based on equation (1) is its practicality. That is, it can readily be repeated by observers based directly on cluster catalogs.

At any rate, to overcome this limitation of our analysis, we constructed a separate sample choosing only those superclusters that have more than five clusters ($N_c > 5$, where $N_c$ is the number of clusters within the supercluster). It is found that 217 superclusters have more than five clusters and that a total of 1492 clusters belong to those 217 superclusters.

First we measure the probability distribution of the cosines of the angles, $\theta$, between the major axes of the superclusters and their member clusters. Figure 2 plots the result as circles with Poissonian error bars. The top panel corresponds to the case in which all 14,007 superclusters are used, while the bottom panel corresponds to that in which only those superclusters with more than five clusters are used. The dotted line in each panel corresponds to the case of no alignment. As can be seen, the distribution, $p(\cos\theta)$, increases with $\cos\theta$ in both panels, revealing a clear signal of the alignment effect. Although the result in the bottom panel shows a less sharp increase, suffering from large errors, the signal is robust at the 99% confidence level. This indicates that the cluster-supercluster alignment effect is not a false signal that originates from an inaccurate derivation of the supercluster major axes, but a real one. The mean values of $\cos\theta$ are found to be 0.54 and 0.52 in the top and bottom panels, respectively.

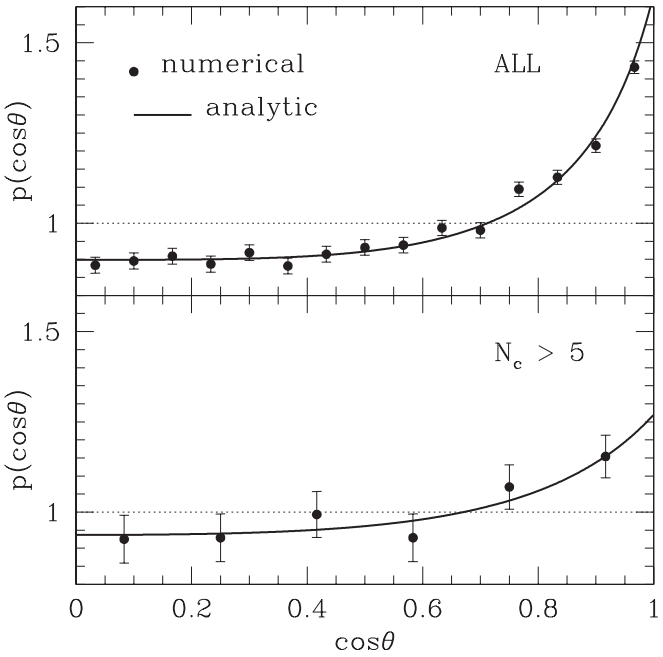


FIG. 2.—Probability density distributions of the cosines of the angles between the major axes of clusters and their superclusters. *Top*, the case in which all 14,007 superclusters are used; *bottom*, the case in which only the 217 superclusters with more than five clusters are used. In each panel, the numerical result is represented by circles with Poissonian errors, while the analytic result (eq. [5]) corresponds to the solid curve. The dotted line corresponds to the case of no alignment.

Now that a robust signal of the cluster-supercluster alignment effect has been found, we may examine how the degree of alignment depends on the cluster properties. First we examine how the average value of cos $\theta$ depends on the cluster mass, $M_c$. Figure 3 plots the result versus the rescaled cluster mass, $\tilde{M} \equiv M_c/M_s$,

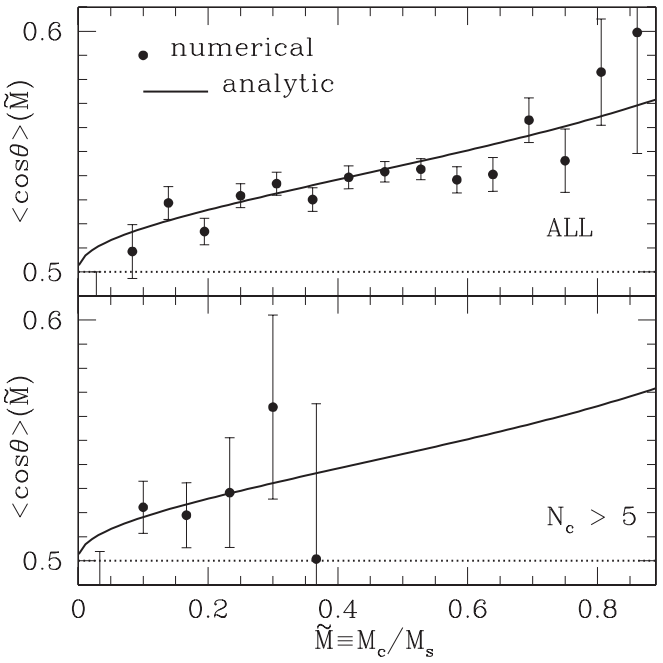


FIG. 3.—Average of the cosines of the angles as a function of cluster mass. *Top*, the case in which all 14,007 superclusters are used; *bottom*, the case in which only the 217 superclusters with more than five clusters are used. In each panel, the circles and solid curves represent the numerical and the analytic results, respectively. The errors are calculated as 1 standard deviation of the cosines of the angles for the case of no alignment. The dotted line corresponds to the case of no alignment.

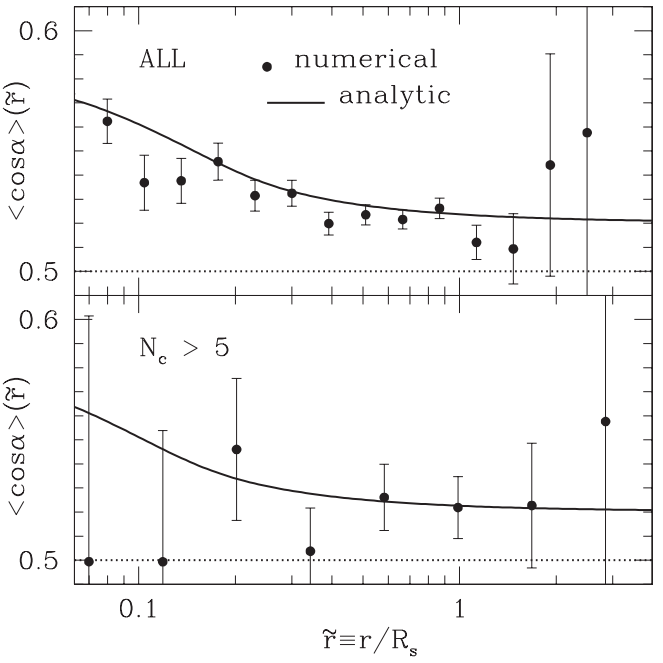


FIG. 4.—Same as Fig. 3, but as a function of the distance from the supercluster center to the cluster center.

as circles with errors that are calculated as 1 standard deviation of cos $\theta$ for the case of no alignment. As can be seen in the top panel, the degree of alignment increases with $\tilde{M}$. A similar trend is also shown in the bottom panel, although it suffers from the large errors.

Second, we examine how the average of cos $\theta$ depends on the separation distance, $r$, from the supercluster center to the cluster center. Figure 4 plots the result versus the rescaled distance $\tilde{r} \equiv r/R_s$. As can be seen in the top panel, the degree of alignment decreases with distance. That is, the closer a cluster is located to the supercluster center, the stronger the alignment effect is.

Third, we examine how the average of cos $\theta$ depends on the cluster ellipticity, $\epsilon$. Here we define the ellipticity of a cluster as $\epsilon \equiv 1 - (\varrho_3^c/\varrho_1^c)^{1/2}$ assuming a prolate shape, where $\varrho_1^c$ and $\varrho_3^c$ are the largest and the smallest eigenvalues of the cluster inertia momentum tensor, respectively. Figure 5 plots the result versus the rescaled ellipticity $\tilde{\epsilon} \equiv \epsilon/\epsilon_0$ (where $\epsilon_0$ is the maximum cluster ellipticity) and reveals that the degree of alignment increases with cluster ellipticity. That is, the more elongated a cluster is, the stronger the alignment effect.

Fourth, we measure the average of cos $\theta$ as a function of the cluster velocity, $v$. Figure 6 plots the result and reveals that the degree of alignment depends very weakly on the cluster velocity. We provide physical explanations for these numerical results in § 3.

## 3. PHYSICAL ANALYSIS

### 3.1. *Hypotheses*

To construct an analytic model for the cluster-supercluster alignment effect, we assume the following:

1. Superclusters form through anisotropic merging of clusters along filaments. In consequence, the major axis of a supercluster tends to be in the direction of the dominant filament. A filament is defined as a one-dimensional object that is collapsed along the major and intermediate principal axes of the local tidal tensor (Zel'dovich 1970; Pogosyan et al. 1998). The direction of a filament thereby is aligned with the minor principal axis of the tidal

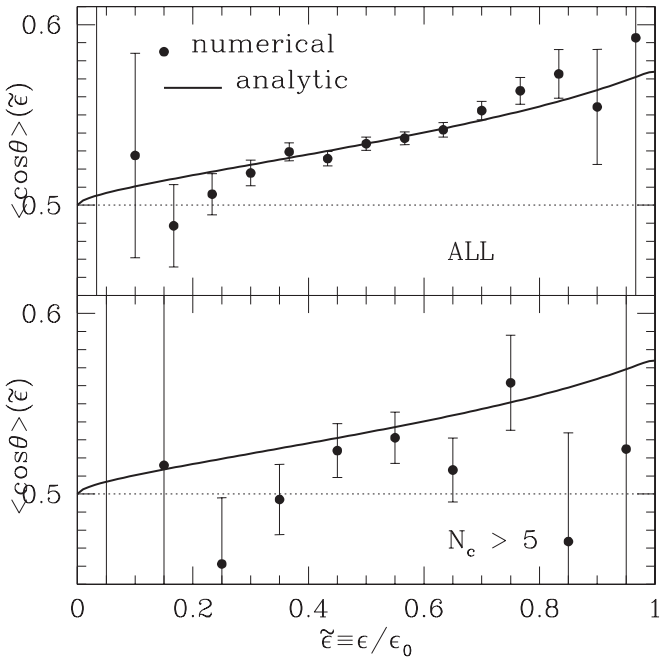


FIG. 5.—Same as Fig. 3, but as a function of cluster ellipticity.

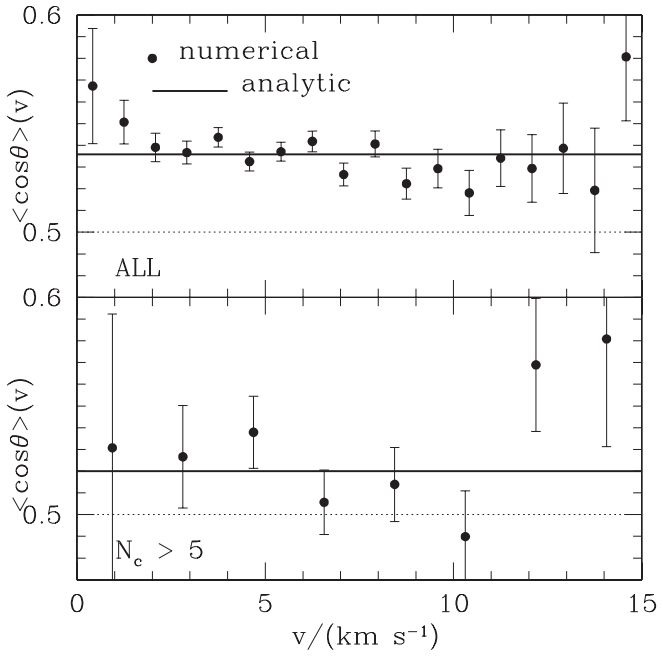


FIG. 6.—Same as Fig. 3, but as a function of cluster velocity.

tensor. Therefore, the major axis of a supercluster tends to be in the direction of the minor principal axis of the tidal tensor.

2. Let $\mathbf{T}^s$ be the tidal tensor field smoothed on the supercluster mass scale, and let $\delta_s \equiv \Delta\rho/\bar{\rho}$ be the linear density contrast of the supercluster, where $\bar{\rho}$ is the mean mass density. Let also $\lambda_1$, $\lambda_2$, and $\lambda_3$ (with $\lambda_1 > \lambda_2 > \lambda_3$) be the three eigenvalues of $\mathbf{T}^s$. The collapse conditions for a supercluster are

$$\delta_s = \lambda_1 + \lambda_2 + \lambda_3 = 1.3, \quad \lambda_1 > \lambda_2 > 0, \quad \lambda_3 < 0. \quad (2)$$

Given that the supercluster has passed the moment of turnaround but not yet virialized, we expect its linear density contrast, $\delta_s$, to be in the range (1, 1.68), where the values of 1 and 1.68 correspond to the linear densities at the moments of turnaround and virialization, respectively (Eke et al. 1996). Here we choose a fiducial value of $\delta_s = 1.3$. The other condition, $\lambda_1 > \lambda_2 > 0$ and $\lambda_3 < 0$, in equation (2) represents the collapse along filaments (Pogosyan et al. 1998).

3. The cluster-supercluster alignment is a reflection of the anisotropic spatial distribution of cluster galaxies in a filament-dominated, weblike cosmic structure. The correlation of the spatial positions of galaxies with the local tidal field can be quantified by the following quadratic equation, which was first suggested by Lee & Kang (2006):

$$\langle x_i^c x_j^c | \hat{\mathbf{T}}^s \rangle = \frac{1-s}{3}\delta_{ij} + s\hat{T}_{ik}^s \hat{T}_{kj}^s, \quad (3)$$

where $\boldsymbol{x}^c \equiv (x_i^c)$ and $\hat{\mathbf{T}}^s = (\hat{T}_{kj}^s) \equiv T_{ik}^s/|\mathbf{T}^s|$ are the rescaled major axis of a galaxy cluster and the unit tidal shear tensor smoothed on the supercluster mass scale, $M_s$. Here the parameter $s \in [-1, 1]$ represents the strength of the correlation between $\boldsymbol{x}^c$ and $\mathbf{T}^s$. If $s = -1$, there is the strongest correlation between $\boldsymbol{x}^c$ and $\hat{\mathbf{T}}^s$. If $s = 1$, there is the strongest anticorrelation between $\boldsymbol{x}^c$ and $\hat{\mathbf{T}}^s$, while if $s = 0$, there is no correlation between them.

4. The conditional probability distribution of $\boldsymbol{x}^c$ provided that the local tidal field is given by $\mathbf{T}^s$ can be approximated as Gaussian:

$$P(\boldsymbol{x}^c|\hat{\mathbf{T}}^s) = \frac{1}{[(2\pi)^3 \det \mathbf{M}]^{1/2}} \exp\left[-\frac{x_i^c(\mathbf{M}^{-1})_{ij}x_j^c}{2}\right] \quad (4)$$

(Lee & Kang 2006), where the covariance matrix $M_{ij} \equiv \langle x_i^c x_j^c | \hat{\mathbf{T}}^s \rangle$ is related to $\hat{\mathbf{T}}^s$ by equation (3).

It is worth mentioning here the difference of cluster-supercluster alignment from galaxy-cluster alignment. In the former case, the primordial tidal field induces the anisotropy in the spatial distribution of galaxies along cosmic filaments, which results in alignment between the major axes of clusters and their superclusters. In the latter case, the tidal field of a virialized cluster halo induces the angular momentum of the cluster galaxies, whose minor axes tend to be aligned with the major axis of its host cluster (Lee et al. 2005). In other words, the alignments between the major axes of cluster galaxies and their host clusters are related to the generation of angular momentum, while the alignments between the major axes of clusters and their host superclusters are related to the filamentary distribution of galaxies.

### 3.2. *Analytic Expressions*

Using the four hypotheses given in § 3.1, we first derive $p(\cos\theta)$ analytically. According to the second hypothesis, this amounts to deriving the probability density distribution of the cosines of the angles between the major axes of clusters and the minor principal axes of the local tidal tensors.

Let us express $\boldsymbol{x}^c$ in terms of spherical polar coordinates in the principal-axis frame of $\mathbf{T}^s$ as $\boldsymbol{x}^c = (x^c \sin\theta\cos\phi, x^c \sin\theta \sin\phi, x^c\cos\theta)$, where $x^c \equiv |\boldsymbol{x}^c|$ and $\theta$ and $\phi$ are the polar and the azimuthal angles of $\boldsymbol{x}^c$, respectively. Then the polar angle $\theta$ is nothing other than the angle between $\boldsymbol{x}^c$ and the minor principal axis of $\mathbf{T}^s$. Now, the probability density distribution of $\cos\theta$

can be derived by integrating equation (4) over $x^c$ and $\phi$ as $p(\cos\theta) = \int_0^{2\pi}\int_0^{\infty} P(x^c, \theta, \phi)x^{c2}\,dx^c\,d\phi$, which leads to

$$p(\cos\theta) = \frac{1}{2\pi}\prod_{i=1}^{3}(1 - s + 3s\hat{\lambda}_i^2)^{-1/2} \times \int_0^{2\pi}\left(\frac{\sin^2\theta\cos^2\phi}{1 - s + 3s\hat{\lambda}_1^2} + \frac{\sin^2\theta\sin^2\phi}{1 - s + 3s\hat{\lambda}_2^2} + \frac{\cos^2\theta}{1 - s + 3s\hat{\lambda}_3^2}\right)^{-3/2} d\phi \quad (5)$$

(Lee & Kang 2006), where $\{\hat{\lambda}_i\}_{i=1}^3$ are the unit eigenvalues of $\hat{\mathbf{T}}$, related to $\{\lambda_i\}_{i=1}^3$ as $\hat{\lambda}_i \equiv \lambda_i/(\lambda_1^2 + \lambda_2^2 + \lambda_3^2)^{1/2}$.

It was in fact Lee & Kang (2006) who first derived equation (5), as an analytic expression for the probability distribution of the alignments between the positions of satellite galaxies in the major-axis orientations of their host galaxies. Here we derive it as an analytic expression for the probability distribution of the alignments between the major axes of clusters and their host superclusters. It is important to note a key difference between the two cases: For the case of galaxy satellites, it is the tidal fields of the *virialized* galactic halos that cause the alignment effect. Therefore, all the eigenvalues $\lambda_1$, $\lambda_2$, and $\lambda_3$ in equation (5) should be positive. For the case of clusters in superclusters, it is the local filaments that collapse, along only two principal axes of the primordial local tidal tensors. Therefore, $\lambda_3$ in equation (5) has a negative value.

This probability distribution is characterized by three independent parameters, $s$, $\lambda_1$, and $\lambda_2$. Once the values of $\lambda_1$ and $\lambda_2$ are determined, then the negative value of $\lambda_3$ is automatically determined by equation (2). Since the values of these three parameters depend on the properties of individual superclusters as well as the local conditions of the initial tidal fields, it may be quite difficult to determine them analytically.

Instead, we determine their average values by fitting equation (5) to the numerical results obtained in § 2. When the numerical result using all superclusters is fitted, the best-fit values of the three parameters are found to be $s = -0.71$, $\lambda_1 = 2.23$, and $\lambda_2 = 0.53$, which gives $\lambda_3 = -1.46$. When the numerical result using only those superclusters with $N_c > 5$ is fitted, it is found interestingly that the best-fit values of the parameters are $s = -0.5$, $\lambda_1 = 2.23$, and $\lambda_2 = 0.53$. Note that the two numerical cases yield the same best-fit values for $\lambda_1$ and $\lambda_2$, although the best-fit values of the correlation parameters are different, $s = -0.71$ and $s = -0.5$.

Figure 2 plots the analytic distributions with these best-fit parameters (*solid lines*) and compares them with the numerical data points. In the top panel, the analytic distribution with $s = -0.71$ is compared with the numerical result obtained in § 2 using all superclusters, while in the bottom panel the analytic distribution with $s = -0.5$ is compared with the numerical result obtained using only those superclusters with more than five clusters ($N_c > 5$). As can be seen, the analytic and the numerical results are in good agreement with each other in both.

It is worth mentioning here that the best-fit values of the three parameters are subject to our fiducial choice of $\delta_s = 1.3$. As mentioned in § 3.1, there is no consensus on the critical linear density of superclusters, unlike the case of clusters. Varying the value of $\delta_s$ from 1.0 to 1.68, we repeated the fitting procedure and found that although the best-fit values of $\lambda_1$ and $\lambda_2$ change by up to 20%, the fitting result itself does not sensitively change with the value of $\delta_s$. Thus, we conclude that our fiducial model is a stable choice.

Now that we have the probability density distribution, $p(\cos\theta)$, we would like to find analytic expressions for $\langle\cos\theta\rangle$ as a function of cluster mass, position, ellipticity, and velocity. The dependence of the correlation parameter $s$ on the cluster mass $M_c$ may be obtained by considering the difference in mass between the cluster and its host supercluster. Strictly speaking, equation (3) is valid when the tidal tensor $\mathbf{T}^s$ and the position vector $\boldsymbol{x}^c$ are smoothed on the same mass scale. In other words, the correlation between $\boldsymbol{x}^c$ and $\mathbf{T}^s$ is expected to be highest when the two smoothing mass scales are the same. In reality, however, $\mathbf{T}^s$ is smoothed on the supercluster mass scale $M_s$, while $\boldsymbol{x}^c$ is smoothed on the cluster mass scale $M_c$. The difference between the two mass scales diminishes the correlation between $\boldsymbol{x}^c$ and $\mathbf{T}^s$.

Let $s_{M_0}$ be the value of the correlation parameter when the tidal field is smoothed on the same cluster mass scale $\mathbf{T}^c$. We expect $s_{M_0} = -1$. Given equation (3), we approximate $s = s(\tilde{M})$ as

$$s(\tilde{M}) \approx s_{M_0}\frac{\langle\hat{T}^s_{ik}\hat{T}^s_{kj}\rangle}{\langle\hat{T}^c_{ik}\hat{T}^c_{kj}\rangle} \approx s_{M_0}\frac{\sigma_s^2}{\sigma_c^2}. \quad (6)$$

Here $\sigma_c$ and $\sigma_s$ represent the rms linear density fluctuations smoothed on the mass scales $M_c$ and $M_s$, respectively. In deriving equation (6), we used the approximation $\langle\hat{T}^c_{ik}\hat{T}^c_{kj}\rangle \approx \langle T^c_{ik}T^c_{kj}\rangle/|\mathbf{T}^c|^2$, which was proved to be valid by Lee & Pen (2001).

Now that the functional form of $s(\tilde{M})$ is found, the average of $\cos\theta$ as a function of $\tilde{M}$ can be calculated from equations (5) and (6) as

$$\langle\cos\theta\rangle(\tilde{M}) = \int_0^{\infty}\cos\theta\, p(\cos\theta; s(\tilde{M}))d(\cos\theta). \quad (7)$$

Figure 3 plots equation (7) with $\lambda_1 = 2.23$ and $\lambda_2 = 0.53$ (*solid line*) and compares it with the numerical result (*circles*) obtained in § 2. For the analytic distribution, the value of $M_s$ is set to be the mean mass of the superclusters found in § 2: $1.26 \times 10^{15}\,h^{-1}\,M_\odot$ (*top*) and $3.69 \times 10^{15}\,h^{-1}\,M_\odot$ (*bottom*). As can be seen, in the top panel the analytic and the numerical results agree with each other excellently. In the bottom panel, although the numerical result suffers from large errors, the analytic prediction is still quite consistent with the numerical result.

The dependence of the correlation parameter $s$ on the distance $r$ between the centers of clusters and their host superclusters can be obtained in a similar way. The correlation between $\boldsymbol{x}^c$ and $\mathbf{T}^s$ in equation (3) becomes strongest when $r = 0$. In reality, however, $r$ always deviates from zero, which will diminish the correlation strength.

Let $s_{r0}$ be the value of the correlation parameter when $r = 0$, which is expected again to be $s_{r0} = -1$. With a similar approximation to that made for equation (6), we find the following formula for $s(r)$:

$$s(r) \approx \frac{s_{r0}}{2}\left[1 + \frac{\langle\hat{T}^c_{ij}(\boldsymbol{x}+\boldsymbol{r})\hat{T}^c_{ij}(\boldsymbol{x})\rangle}{\langle\hat{T}^c_{ij}(\boldsymbol{x})\hat{T}^c_{ij}(\boldsymbol{x})\rangle}\right] \approx \frac{s_{r0}[1 + \tilde{\xi}_c(r)]}{2}, \quad (8)$$

where $\tilde{\xi}_c(r)$ represents the two-point density correlation rescaled to satisfy the condition that $\tilde{\xi}_c(0) = 1$. Since the distance

$r$ is an Eulerian quantity, unlike the mass $M_s$, we use the Eulerian filtering radius of 2 $h^{-1}$ Mpc, the typical cluster size, to convolve the correlation function $\tilde{\xi}_c$. Here the factor of $\frac{1}{2}$ comes from the average decreases of the correlation parameter due to the mass difference between the clusters and their host superclusters.

Now that the functional form $s(r)$ is known, the average of cos $\theta$ as a function of $r$ can be calculated through equations (5) and (8) as

$$\langle \cos\theta \rangle(r) = \int_0^\infty \cos\theta\, p(\cos\theta; s(r)) d(\cos\theta). \quad (9)$$

Figure 4 plots equation (9) (*solid line*) as a function of the rescaled distance, $\tilde{r} \equiv r/R_s$, and compares it with the numerical result (*circles*) obtained in § 2. For the analytic distribution, the value of $R_s$ is set to be the mean Lagrangian radius of superclusters found in § 2, using the relation $R_s = [3\bar{M}_s/(4\pi\bar{\rho})]^{1/3}$. As can be seen, the analytic and the numerical results agree quite well.

Regarding the dependence of $s$ on the cluster ellipticity, $\epsilon$, although it is predicted qualitatively in our theoretical model that the degree of the alignment will increase with ellipticity, the quantitative functional form of $s(\epsilon)$ is quite difficult to determine analytically, since the cluster ellipticities are sensitively vulnerable to modifications caused by nonlinear merging and infall processes.

Instead of the analytic approach, we use numerical fitting to determine the functional form of $s(\epsilon)$. Let $s_{\epsilon 0}$ represents the value of $s$ when the cluster ellipticity has the maximum value, $\epsilon_0$. It is expected again that $s_{\epsilon 0} = -1$. We find that the following formula gives a good fit to the numerical results:

$$s(\tilde{\epsilon}) = s_{\epsilon 0}\tilde{\epsilon}^{1/2}. \quad (10)$$

Since $\epsilon_0$ is defined as the maximum ellipticity, $s(\tilde{\epsilon})$ has the extreme value of $-1$ at $\tilde{\epsilon} = 1$. Note that the value of $\epsilon_0$ is not fixed, but sample-dependent. Here, the Millennium Run data we use (Springel et al. 2005) yield $\epsilon_0 = 0.7$, but a different sample could yield a different value.

Now that the functional form of $s(\tilde{\epsilon})$ has been found, the average of cos $\theta$ as a function of $\tilde{\epsilon}$ can be calculated from equations (5) and (10) as

$$\langle \cos\theta \rangle(\tilde{\epsilon}) = \int_0^\infty \cos\theta\, p(\cos\theta; s(\tilde{\epsilon})) d(\cos\theta). \quad (11)$$

The comparison between the analytic result (eq. [11]) and the numerical data points shows good consistency, as can be seen in Figure 5.

Regarding the dependence of $s$ on the cluster velocity $v$, no strong dependence is expected in our model, since the primordial tidal field is uncorrelated with the velocity field (Bardeen et al. 1986). Therefore, we model it as having a uniform distribution $\langle \cos\theta \rangle(v) = \langle \cos\theta \rangle$. The average value, $\langle \cos\theta \rangle$, is found to be 0.54 when $s = -0.71$ (Fig. 6, *top*), while it is 0.52 when $s = -0.5$ (*bottom*). As can be seen in Figure 6, the analytic and the numerical results are consistent with each other.

## 4. DISCUSSION AND CONCLUSION

In the context of the standard cosmic-web picture of large-scale structure, we have constructed a parametric model for the alignment of cluster-sized halos with their host superclusters. The underlying assumption is that cluster-supercluster alignment reflects the spatial distribution of matter as it is organized along filamentary structures by the primordial tidal field. The parameters of the analytic model represent the dominance of filaments and the spatial coherence of the initial tidal field.

We showed that the analytic model provides a good fit to orientation data derived from mass-limited halo samples of a ΛCDM Hubble volume simulation. After fitting the three free parameters using the overall distribution of cluster-supercluster alignment angles, the model can simultaneously match the behavior of the mean alignments as a function of relative mass, cluster position within the supercluster, and cluster ellipticity. No trend with cluster velocity is predicted or measured in the simulation.

It is worth discussing a couple of simplified assumptions on which our theoretical model is based. First, we have used the friends-of-friends algorithm to identify superclusters in the $N$-body simulation data. Unlike the case of virialized clusters, however, there is no established consensus on how to define superclusters. Different supercluster identification algorithms could result in different multiplicities, masses, and shapes of superclusters, which would in turn affect our results.

Second, we assumed that the filaments correspond to the Lagrangian regions where only the largest and the second-largest eigenvalues of the local tidal tensor are positive. Although this definition of a filament is consistent with the picture in the Zel'dovich approximation, it is obviously an oversimplification of reality. A more realistic definition and treatment of cosmic filaments will be necessary to refine the model.

Another issue that we would raise is the possibility of using the cluster-supercluster alignment effect as a cosmological probe. We have shown that the phenomena of cluster-supercluster alignments are closely related to the dominance of filaments—the weblike distribution of galaxies on very large scales. The dominance of filaments is in turn related to the spatial correlations of the primordial tidal field, which depend sensitively on the slope of the initial power spectrum on the supercluster scale. Thus, by measuring the degree of cluster-supercluster alignment, it might be possible to constrain the slope of the initial power spectrum in a complementary way.

Finally, we conclude that our model for cluster-supercluster alignments provides a theoretical framework within which the distribution of cosmic structures on the largest scales can be physically understood and quantitatively described.

We are grateful to the anonymous referee, who helped us improve the original manuscript. We are also grateful for the warm hospitality of Y. Suto and the University of Tokyo, where this work was initiated. J. L. also thanks D. Park for useful help. J. L. is supported by research grant R01-2005-000-10610-0 from the Basic Research Program of the Korea Science and Engineering Foundation. J. L. was also supported by the Research Settlement Fund for new faculty of Seoul National University. A. E. E. acknowledges support from the Miller Institute for Basic Research in Science at the University of California, Berkeley, from NSF Information Technology Research grant ACI 01-21671, and from NASA Astrophysics Theory Program grant NAG 5-13378.

REFERENCES

Agustsson, I., & Brainerd, T. G. 2006, ApJ, 644, L25
Atlay, G., Colberg, J. M., & Croft, R. A. C. 2006, MNRAS, 370, 1422
Bardeen, J. M., Bond, J. R., Kaiser, N., & Szalay, A. S. 1986, ApJ, 304, 15
Basilakos, S. 2003, MNRAS, 344, 602
Basilakos, S., Plionis, M., Yepes, G., Gottlöber, S., & Turchaninov, V. 2006, MNRAS, 365, 539
Bond, J., R., Kofman, L., & Pogosyan, D. 1996, Nature, 380, 603
Brainerd, T. G. 2005, ApJ, 628, L101
Busha, M. T., Evrard, A. E., Adams, F. C., & Wechsler, R. H. 2005, MNRAS, 363, L11
Dubinski, J. 1998, ApJ, 502, 141
Eke, V., Cole, S., & Frenk, C. S. 1996, MNRAS, 282, 263
Evrard, A. E., et al. 2002, ApJ, 573, 7
Faltenbacher, A., Gottlöber, S., Kerscher, M., & Müller, V. 2002, A&A, 395, 1
Kalinkov, M., Valtchanov, I., & Kuneva, I. 1998, ApJ, 506, 509
Kang, X., Mao, S., Gao, L., & Jing, Y. P. 2005, A&A, 437, 383
Kasun, S. F., & Evrard, A. E. 2005, ApJ, 629, 781
Knebe, A., Gill, S. P. D., Gibson, B. K., Lewis, G. F., Ibata, R. A., & Dopita, M. A. 2004, ApJ, 603, 7
Lee, J., & Kang, X. 2006, ApJ, 637, 561
Lee, J., Kang, X., & Jing, Y. P. 2005, ApJ, 629, L5
Lee, J., & Pen, U.-L. 2001, ApJ, 555, 106
Libeskind, N. I., Frenk, C. S., Cole, S., Helly, J. C., Jenkins, A., Navarro, J. F., & Power, C. 2005, MNRAS, 363, 146
Nagamine, K., & Loeb, A. 2003, NewA, 8, 439
Onuora, L. I., & Thomas, P. A. 2000, MNRAS, 319, 614
Pereira, M. J., & Kuhn, J. R. 2005, ApJ, 627, L21
Plionis, M. 2002, in Modern Theoretical and Observational Cosmology, ed. M. Plionis & S. Cotsakis (Dordrecht: Kluwer), 299
———. 2004, in IAU Colloq. 195, Outskirts of Galaxy Clusters, ed. A. Diaferio (Cambridge: Cambridge Univ. Press), 19
Plionis, M., & Basilakos, S. 2002, MNRAS, 329, L47
Plionis, M., Benoist, C., Maurogordato, S., Ferrari, C., & Basilakos, S. 2003, ApJ, 594, 144
Pogosyan, D., Bond, J. R., Kofman, L., & Wadsley, J. 1998, in Wide Field Surveys in Cosmology, ed. S. Colombi, Y. Mellier, & B. Raban (Gif-sur-Yvette: Ed. Frontières), 61
Shapley, H. 1930, Bull. Harvard Coll. Obs., No. 874, 9
Springel, V., et al. 2005, Nature, 435, 629
Valtonen, M. J., Teerikorpi, P., & Argue, A. N. 1978, AJ, 83, 135
van Haarlem, M., & van de Weygaert, R. 1993, ApJ, 418, 544
West, M. J. 1989, ApJ, 347, 610
West, M. J., Villumsen, J. V., & Dekel, A. 1991, ApJ, 369, 287
Zel'dovich, Ya. B. 1970, A&A, 5, 84
Zentner, A. R., Kravtsov, A. V., Gnedin, O. Y., & Klypin, A. A. 2005, ApJ, 629, 219